Simulation of loss cone overfilling and atmospheric precipitation induced by a fine-structured chorus element

M. Hanzelka[1,2], O. Santolík[1,3], I. Kolmašová[1,3]

[1]Department of Space Physics, Institute of Atmospheric Physics, Czech Academy of Sciences, Prague,

Czech Republic

[2]Center for Space Physics, Boston University, Boston, Massachusetts, USA

[3]Faculty of Mathematics and Physics, Charles University, Prague, Czech Republic

Key Points:

- Test particle simulations and nonlinear growth theory are used to simulate loss of energetic electrons interacting with a chorus element
- Nonlinear cyclotron resonant interaction of electrons with high-amplitude chorus can break the strong diffusion limit
- Subpacket modulation of chorus elements gives rise to a corresponding weaker modulation in precipitating electron fluxes

Corresponding author: M. Hanzelka, `mha@ufa.cas.cz`

Abstract

Nonlinear wave-particle interactions contribute to the acceleration and precipitation of electrons in the outer radiation belt. Recent simulations and spacecraft observations suggest that oblique whistler-mode chorus can cause loss cone overfilling through nonlinear Landau resonance and thus break the strong diffusion limit of quasilinear theories. Here we show with test-particle simulations that a single element of parallel-propagating chorus can also break the diffusion limit through nonlinear cyclotron resonance, as long as its amplitude remains high. This is due to the strong scattering at low pitch angles caused by individual chorus subpackets. We further demonstrate that the subpacket modulations create a discernible pattern in the precipitating electron fluxes, with peaks correlated with the largest subpackets. Such flux patterns may be connected to weak micropulsations within diffuse auroras.

Plain Language Summary

It has been recently shown that the flux of electrons precipitating into the atmosphere from the Earth's outer radiation belt can become higher than the flux of trapped electrons. Such large precipitated fluxes contradict the strong diffusion limit from older theories explaining the precipitation by quasilinear wave-particle resonant interactions. This superfast precipitation was connected to whistler-mode (right-hand polarized) electromagnetic waves with oblique wave vectors with respect to the terrestrial magnetic field lines. We demonstrate by means of test-particle simulations that high-amplitude whistler waves with wave vectors parallel to the background magnetic field can also break the strong diffusion limit. Furthermore, if the waves exhibit fine amplitude modulations, as is the case with the chorus emission, these modulations will be reflected in the evolution of the precipitating flux and may appear as micropulsations in auroras.

1 Introduction

The rapid acceleration and loss of outer radiation belt electrons are known to be caused by resonant interactions with plasma waves, with whistler-mode waves being a significant driver (Summers et al., 2007; Baker, 2021). In recent years, the role of nonlinear scattering on short timescales has been actively studied both numerically and experimentally (Foster et al., 2017; Kubota & Omura, 2018; da Silva et al., 2018; Allanson et al., 2020; Hsieh et al., 2022). Nonlinear interactions are associated with large am-

plitude waves, of which the lower-band chorus emissions are an important example. These whistler-mode emissions occur at frequencies between $0.1\,\Omega_e$ and $0.5\,\Omega_e$ (Ω_e being the local electron gyrofrequency) and are characterized by trains of chirping elements in time-frequency spectrograms, reaching magnetic field amplitudes up to about $1\,\mathrm{nT}$ (Li et al., 2011; Santolík et al., 2014; Taubenschuss et al., 2015). Each element is further modulated in amplitude and often exhibits a characteristic subpacket structure (Santolík, Gurnett, et al., 2003; Santolík, 2008; Crabtree et al., 2017) that affects the efficiency of wave-particle interactions (Hiraga & Omura, 2020; Zhang et al., 2020).

Individual elements of chorus are associated with microbursts of precipitating electron flux (Hikishima et al., 2010; Breneman et al., 2017). The electron energy in such bursts reaches values from tens of keV to units of MeV (Lorentzen et al., 2001; Tsurutani et al., 2013). In polar regions, the precipitating electrons contribute to the formation of pulsating auroras (Miyoshi et al., 2020; Kawamura et al., 2021). Observations of Ozaki et al. (2018) revealed some correlations between the fine subpacket structure of chorus and 10^{-3}–$10^{-2}\,\mathrm{s}$ micropulsation in auroral intensity.

The flux of precipitating electrons is expected to comply with the strong diffusion limit derived from the quasilinear theory (Kennel & Petschek, 1966). In this limit, a large pitch-angle diffusion rate transports electrons so fast that the precipitating flux just below the loss cone boundary nearly matches the trapped electron flux above the boundary. Recently, Zhang et al. (2022) discovered signs of loss cone overfilling in the Arase and ELFIN spacecraft data – defined by precipitating fluxes exceeding trapped fluxes – and demonstrated that nonlinear interactions with oblique whistler waves are the probable cause of the strong diffusion limit violation. According to their theory, the turbulent motion of phase space density (PSD) at low pitch angles caused by a strong $n = 0$ (Landau) resonance moves high-density volumes of electrons from lower parallel velocities $v_\parallel$ and exchanges them with low-density phase space volume at higher $v_\parallel$. A density peak is formed at low equatorial pitch angles inside the loss cone, resulting in a major burst of precipitating flux.
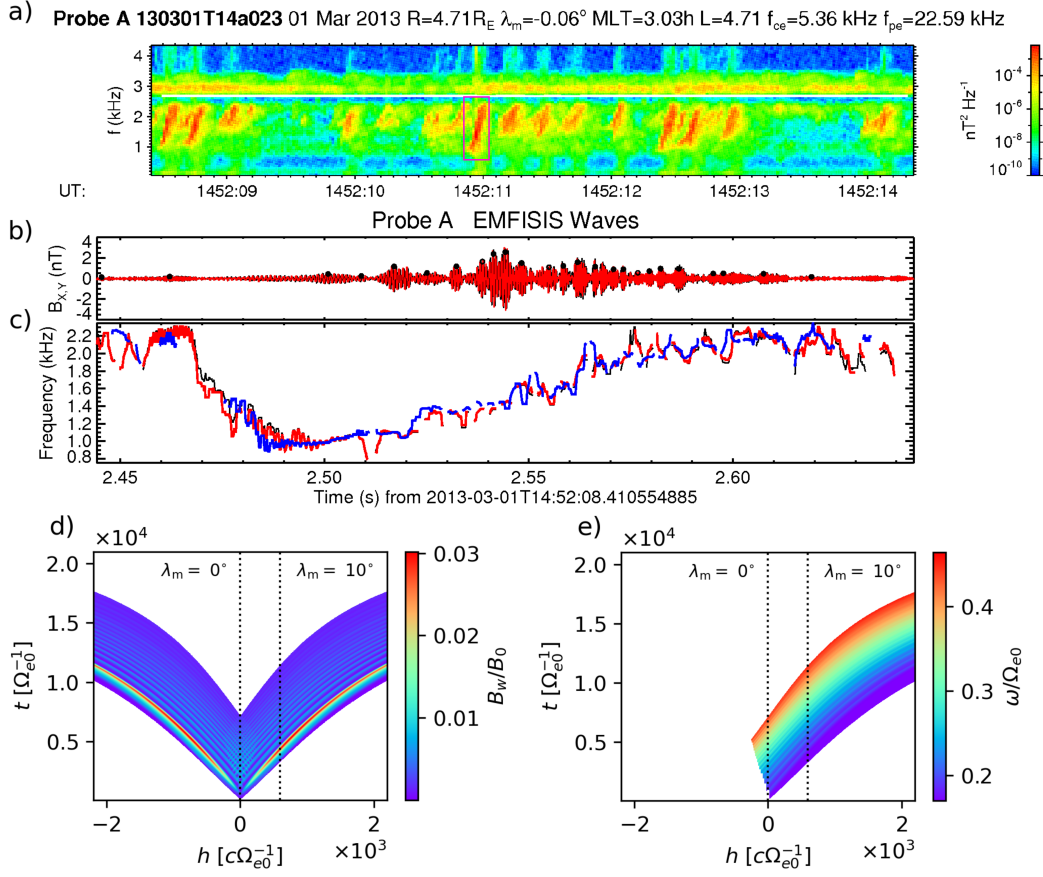
Here we consider the possibility of loss cone overfilling due to $n = 1$ (fundamental cyclotron) resonance with parallel-propagating chorus elements. Using the chorus model of Hanzelka et al. (2020) and test-particle methods to obtain a high-resolution perturbed velocity distribution (Hanzelka et al., 2021), we investigate the effects of an intense lower-

band chorus element and its amplitude modulations. It is shown that nonlinear cyclotron resonant interactions can cause a significant violation of the strong diffusion limit on sub-packet timescales, on the order of 10^{-2} s. We then map the near-equatorial phase space density to atmospheric altitudes and assess the precipitating electron flux. The precipitation exhibits modulations associated with subpackets, supporting the observations of micropulsations in auroral intensity by Ozaki et al. (2018).

2 Models and methods

To construct an electromagnetic wavefield of a lower-band chorus, we use the 1D model of a single rising-tone element of Hanzelka et al. (2020) with improvements introduced by Hanzelka et al. (2021). The model is based on the nonlinear growth theory (Omura, 2021). The input parameters for the model are inspired by Van Allen Probe A burst-mode observation, presented in Figures 1a,b in the form of time-frequency spectrogram and waveforms of perpendicular magnetic fluctuations. The element is about 160 ms long and spans a frequency range from 900 Hz ($0.17\,\Omega_{\mathrm{e}}$) to 2300 Hz ($0.43\,\Omega_{\mathrm{e}}$). The instantaneous frequency shown in Figure 1c was obtained from the analytic signal (Santolík et al., 2014) and exhibits an irregular growth.

The evolution of amplitudes B_{w} and frequencies ω of the model wavefield is presented in time-space plots in Figures 1. In the numerical solution of model equations (see the appendix in Hanzelka et al. (2021) for details), we assumed a dipole model of the background magnetic field with equatorial field strength at $L = 1$ set to $B_{\mathrm{surf}} = 2 \cdot 10^{-5}$ T to fit the observed equatorial gyrofrequency $f_{\mathrm{ce0}} = 5.36\mathrm{kHz} \sim \Omega_{\mathrm{e0}} = 3.37 \cdot 10^4\,\mathrm{s}^{-1}$ at $L = 4.71$. Other parameters are as follows: initial frequency $\omega_0/\Omega_{\mathrm{e0}} = 0.17$, final frequency $\omega_{\mathrm{f}}/\Omega_{\mathrm{e0}} = 0.44$, plasma frequency $\omega_{\mathrm{pe}}/\Omega_{\mathrm{e0}} = 4.1$ (kept constant along the field line for simplicity), hot plasma frequency $\omega_{\mathrm{phe}}/\Omega_{\mathrm{e0}} = 0.375$ (resulting in a hot/cold electron density ratio of $0.8\,\%$), characteristic perpendicular velocity of a bi-Maxwellian distribution $V_{\perp 0}/c = 0.45$ (c being the speed of light), relativistic parallel thermal velocity $U_{\mathrm{t}\|0}/c = 0.2$, electron hole depth $Q = 0.75$ and time scale parameter $\tau = 0.5$. The model equations were solved up to the field-aligned distance $h_{\mathrm{f}} = 2200\,c\Omega_{\mathrm{e0}}^{-1}$, which translates to a magnetic latitude of $\lambda_{\mathrm{f}} = 37°$. As a shortcoming of the sequential nature of the numerical model, the first subpacket is significantly stronger than the others.

Figure 1. Example chorus element and the wavefield model. a) Magnetic power spectrogram of chorus emission created from 6-second burst-mode data measured by the EMFISIS instrument on Van Allen Probe A, processed by the signal analysis methods of Santolík, Parrot, and Lefeuvre (2003). The magenta box highlights the time and frequency range of the example element. b) Perpendicular magnetic field waveform of the highlighted element. The black line in the background corresponds to the total wave magnetic field. Black dots mark the peaks of individual subpackets. c) Instantaneous wave frequencies. The red line corresponds to the perpendicular field, the blue line to the parallel field, and the total field is plotted in black. Data corresponding to amplitudes below 50 pT are removed. In the first 40 ms, the high-frequency tail of the previous element is still visible. The waveform processing follows the methods used by Santolík et al. (2014). d) Magnetic field amplitudes obtained from the model of Hanzelka et al. (2020), normalized to the equatorial dipole field strength. Input parameters are given in the text. e) Frequencies in the wavefield model. The symmetric, left-propagating part of the field is hidden to reveal the behavior near the equator.

To make our numerical investigation relevant for future experimental research, we need to take the energy range of available spacecraft instrumentation into account. To give some examples, the ELFIN EPD (Energetic Particle Detector, Angelopoulos et al. (2020)) does not detect particles below 50 keV, and the energy range of DEMETER IDP (Instrument for the Detection of Particles, Sauvaud et al. (2006)) starts at 70 keV. These restrictions are brought into comparison with minimum cyclotron resonant energies in Figure 2a. We can see that despite the relatively low initial frequency of the model element (compare with spectral characteristics of chorus presented by Teng et al. (2019)), only off-equatorial waves can reach resonance energies above the lower threshold of the aforementioned particle detectors. Higher resonant energies are possible away from the loss cone (where perpendicular velocity $v_\perp$ becomes the dominant component) or in low density troughs, as shown in Figure 2b. The minimum resonant energies E_k were derived from the cold plasma dispersion and the $n = 1$ cyclotron resonance condition as (see also Supporting Information, Text S1)

$$
\begin{aligned}
E_k &= mc^2 \left(\frac{1}{\sqrt{1 - V_R^2(0)/c^2}} - 1 \right), \\
\frac{V_R(0)}{c} &= \frac{ck\omega - \Omega_e \sqrt{\Omega_e^2 + c^2 k^2 - \omega^2}}{\Omega_e^2 + c^2 k^2}, \\
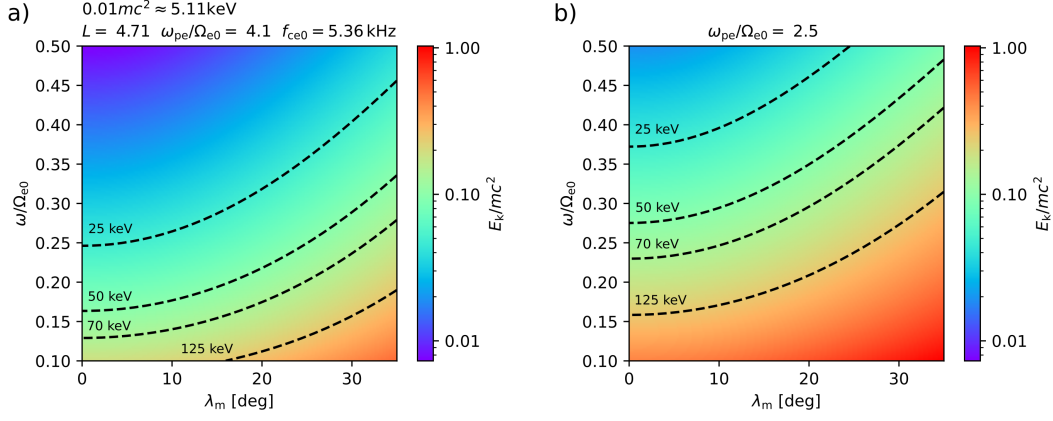c^2 k^2 &= \omega^2 + \frac{\omega \omega_{pe}^2}{\Omega_e - \omega},
\end{aligned}
\tag{1}
$$

where m stands for electron mass, k is the whistler-mode wavenumber and $V_R(0)$ is the parallel resonance velocity for $v_\perp = 0$. A commonly used approximate formula

$$
E_k \approx \frac{mc^2}{2} \frac{(\Omega_e - \omega)^3}{\omega \omega_{pe}^2}
\tag{2}
$$

can be obtained under the non-relativistic conditions $c^2 k^2 / \omega^2 \gg 1$, $V_R/c \ll 1$.

Perturbations to the hot electron velocity distribution due to wave-particle interactions are obtained with backward-in-time test-particle simulations (Nunn & Omura, 2015; Hanzelka et al., 2021). In order to capture the full extent of the interaction, the particle tracing must start upstream at the h-value corresponding to the source of the last subpacket. We set the initial position of the backtraced particle to $h_f = -268 \, c\Omega_{e0}^{-1}$ and shift the initial times from $t_f = 500 \, \Omega_{e0}^{-1}$ to $t_f = 21000 \, \Omega_{e0}^{-1}$ with steps of $500 \, \Omega_{e0}^{-1}$. The unperturbed distribution is bi-Maxwellian in momenta and preserves – in agreement with Liouville's theorem – the PSD along adiabatic particle trajectories:

$$
f(u_\parallel, u_\perp, h) = \frac{n_{he}(h)}{(2\pi)^{3/2} U_{t\parallel}(h) U_{t\perp}^2(h)} \exp \left(-\frac{u_\parallel^2}{2 U_{t\parallel}^2(h)} - \frac{u_\perp^2}{2 U_{t\perp}^2(h)} \right),
\tag{3}
$$

Figure 2. a) Minimum resonant energies of cyclotron interaction between whistler waves and electrons in a dipole magnetic field at $L = 4.71$. The gyrofrequency and plasma frequency are taken from the spacecraft measurement in Figure 1. Some representative energy contours are plotted as black dashed lines. The relativistic formula from Equation 1 was used in the computation. b) Similar to previous panel, but with a lower plasma frequency.

where

$$U_{t\parallel}(h) = U_{t\parallel}(0)\,, \ U_{t\perp}(h) = W(h)U_{t\perp}(0)\,, \ n_{he}(h) = W^2(h)n_{he}(0)\,,$$

$$W(h) = \left(1 + \left(1 - \frac{B_0(0)}{B_0(h)}\right)\left(\frac{U_{t\perp}^2(0)}{U_{t\parallel}^2(0)} - 1\right)\right)^{-\frac{1}{2}} \tag{4}$$

with $U_{t\perp}(0) = \sqrt{2/\pi}\,\gamma V_{\perp 0}$, where $V_{\perp 0}$ comes from the nonlinear growth theory (refer to the wave model input parameters listed near the beginning of this section). Additionally, the loss cone is assumed to be empty before the interaction, i.e.,

$$f(u_\parallel, u_\perp, h) = 0 \text{ for } \alpha \gtrless \alpha_{loss}(h)\,, \tag{5}$$

$$\alpha_{loss} = \frac{\pi}{2} \pm \left(\frac{\pi}{2} - \arcsin\sqrt{\frac{B_0(h)}{B_0(h_m)}}\right)\,, \tag{6}$$

where we use the $+$ and $>$ signs for particles propagating against the background field. $B_0(h_m)$ is the magnetic field strength at the point where electrons stop being able to mirror because of collisions with dense atmospheric layers. At length scales of high-L field lines, the thickness of atmospheric layers becomes negligible, and so we can approximate h_m by the length of the field line measured from the magnetic equator to the Earth's surface.

The velocity distribution is sampled uniformly at each final point (t_f, h_f) by 64 points in gyrophase φ, 128 points in parallel velocities ranging from 0 to $-0.6\,c$, and 128 points

147 in perpendicular velocities ranging from 0 to $0.06\,c$. The advantage of the backwards-

148 in-time tracing is the option to choose any section of the phase space without regard to

149 the initial configuration of particles before the resonant interaction, allowing us to fo-

150 cus on the loss cone and maintain a very high velocity-space resolution. Furthermore,

151 the resulting PSD is essentially noiseless. On the other hand, each time-space point re-

152 quires a new simulation run. The time step of a relativistic Boris algorithm with phase

153 correction (Higuera & Cary, 2017; Zenitani & Umeda, 2018) is set to $\Delta t = 0.02\,\Omega_{\mathrm{e0}}^{-1}$

154 to ensure tolerable errors over the whole range of latitudes.

155 To quantify the filling of the loss cone and atmospheric precipitation, we first carry

156 out the coordinate transform $(v_\parallel,\, v_\perp) \to (E_{\mathrm{k}},\, \alpha)$. 128 logarithmically spaced energy

157 bins are used, ranging from $10^{-3}\,mc^2$ to $10^0\,mc^2$. Binning in pitch angle is uniform, with

158 128 points from $180°$ to $\alpha_{\mathrm{loss}}(h_{\mathrm{f}}) = 175.8°$. The energy–pitch-angle distribution at the

159 precipitation level (approximated by the Earth's surface) is sampled with the same num-

160 ber of bins, but angles run down to $90°$. The PSD is obtained by numerically integrat-

161 ing adiabatic particle trajectories from the Earth's surface to h_{f} and mapping interpo-

162 lated values back to the surface. Linear interpolation in time is used, while angles are

163 interpolated to the nearest neighbor (and energy is conserved). The adiabatic tracing

164 is done for 1000 uniformly spaced time points from $t \approx 8000\,\Omega_{\mathrm{e0}}^{-1}$ to $t \approx 48000\,\Omega_{\mathrm{e0}}^{-1}$.

165 This range was chosen based on the period spanned by t_{f} and on the time of flight of in-

166 dividual particles. Finally, the differential of the omnidirectional flux is related to the

167 phase space density as (in the approximation $E_{\mathrm{k}} \ll mc^2$)

$$\mathrm{d}F(E_{\mathrm{k}}, \alpha, t) = 2f(E_{\mathrm{k}}, \alpha, t)E_{\mathrm{k}}\sin\alpha\,\mathrm{d}\alpha\,\mathrm{d}E_{\mathrm{k}}\,. \tag{7}$$

168 Precipitating electron flux across energies $F(E_{\mathrm{k}}, t)$ is then obtained by integration over

169 α and the total flux $F(t)$ results from a second integration over E_{k}.

3 Results

171 We start our investigation by looking at snapshots from the evolution of the ve-

172 locity distribution integrated over gyrophase, presented in Figure 3. At $t = 2000\,\Omega_{\mathrm{e0}}^{-1}$

173 (Fig. 3a), we can see that the loss cone portion corresponding to the resonant energies

174 of the first subpacket (for $v_\parallel/c$ between -0.42 and -0.32) has been filled almost homo-

175 geneously, and the scattering by the second subpacket is starting to appear at lower en-

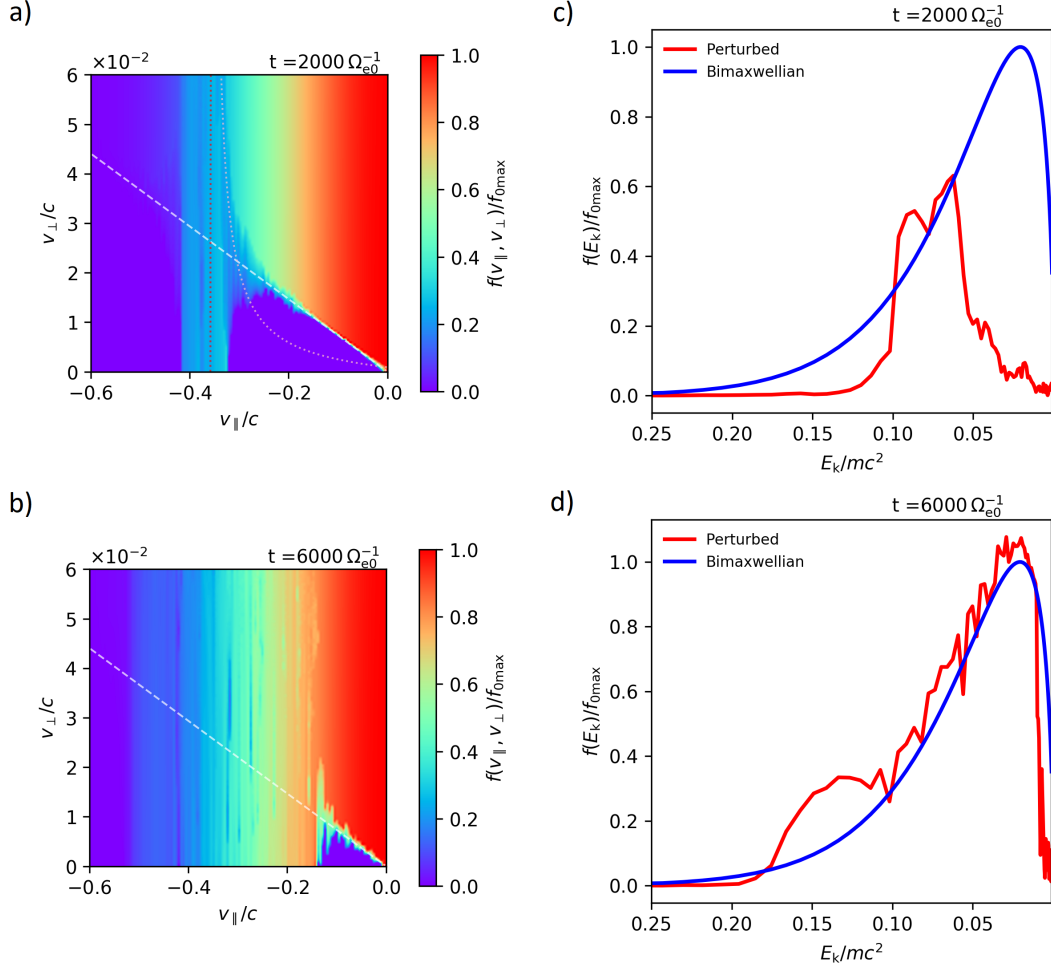176 ergies. At these low pitch angles, the resonance velocity becomes amplitude-dependent

177   and ζ-dependent (where ζ is the difference between the gyrophase and the wave phase),

178   and thus the first subpacket may also cause trapping at lower energies and slightly mod-

179   ify the scattering process – see Albert et al. (2021) and the Supporting Information (SI)

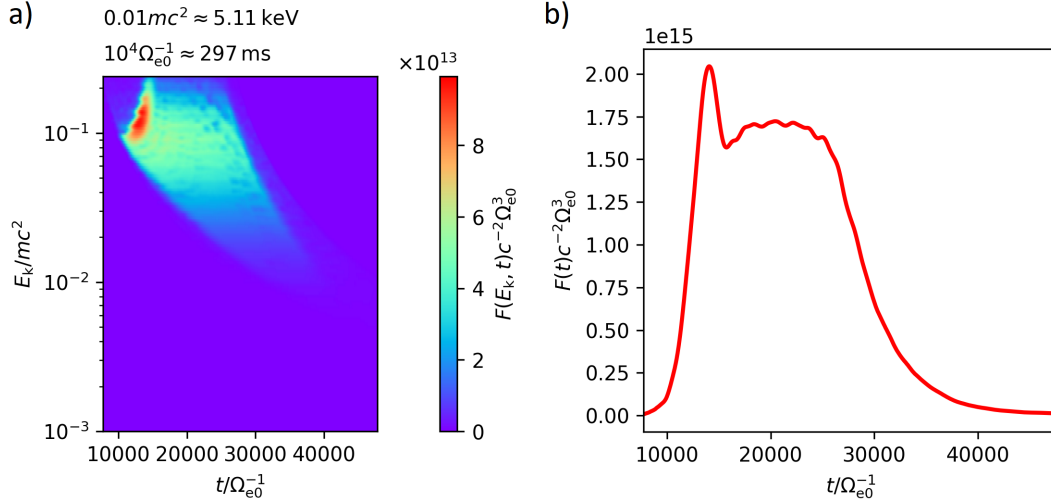180   for more details on this anomalous behavior.

181   As we move forward in time to $t = 6000\,\Omega_{e0}^{-1}$ (Fig. 3b), we start seeing particles

182   that have interacted with the high-frequency end of the chorus element, causing scat-

183   tering at low energies. Below $v_\parallel \approx -0.15\,c$ ($E_k \approx 6\,\mathrm{keV}$), the scattering is not strong

184   enough to completely fill the loss cone. There are no significant PSD decreases outside

185   the loss cone. As expected from the results presented by Hanzelka et al. (2021), the de-

186   pletion stripes associated with electron holes diminish below $v_\perp \approx 0.1\,c$. The full step-

187   by-step evolution of the perturbed PSD can be found in the Supporting Information as

188   Movie S1.

189   To quantify the filling of the loss cone, we transform the PSD to energy and pitch

190   angle coordinates and integrate from α_{loss} to $\alpha = 180°$. Figures 3c,d compare the per-

191   turbed distribution to a bi-Maxwellian with a full loss cone (i.e. distribution from Equa-

192   tion 3 without Eq. 5). Scattering induced by the first subpacket causes a major over-

193   filling at resonant energies, reaching more than double the bi-Maxwellian PSD value. This

194   could be seen as a side effect of the overestimation of B_w in the first subpacket. How-

195   ever, perturbations plotted in Figures 3c,d show that the low-amplitude, high-frequency

196   portion of the chorus element also causes overfilling, although only fractional. At the late

197   stage of the evolution, where the amplitudes of off-equatorial subpackets fall below $10^{-3}\,B_0(h)$,

198   the PSD in the loss cone matches the bi-Maxwellian (see the entire time evolution pre-

199   sented in Movie S2 in the SI). This state corresponds to the strong diffusion limit from

200   the quasilinear theory.

201   The discovery of loss cone overfilling might be surprising at first, given that the res-

202   onant electrons at low pitch angles are supposed to experience only negligible variation

203   in parallel velocity (Zhang et al., 2022), and thus should not be able to access the high-

204   density regions of electron distribution at lower energies. However, when the wavefield

205   reaches amplitudes on the order of $1\,\%$ of the background field, the particles can expe-

206   rience a large change in pitch angle with a comparatively minor increase in energy (Summers

207   et al. (1998); see also the additional discussion and Figure S1 in the Supporting Infor-

208   mation). If the hot electron distribution is highly anisotropic, which is a common assump-

Figure 3. a,b) Snapshots of the hot electron distribution $f(v_\parallel, v_\perp, h = -268\, c\Omega_{e0}^{-1})$ at low perpendicular velocities due to the interaction with chorus element from Figures 1d,e. The dashed white line determines the local boundary of the loss cone. The dark red dotted curve in panel a) represents the resonance velocity for $\omega/\Omega_{e0} = 0.2$ (mean frequency of the second subpacket). The pink dotted curve stands for a ζ-dependent resonance velocity $V_R^{\zeta=\pi}$ with $B_w/B_0 = 7.5 \cdot 10^{-3}$, which is supposed to reflect scattering anomalies at low pitch angles; see the Supporting Information for additional details. c,d) Red line: Snapshots of the energy distribution $f(E_k, h = -268\, c\Omega_{e0}^{-1})$, obtained by coordinate transformation of the data from panels a) and b) and integration over the loss cone's angular extent. Blue line: the unperturbed bi-Maxwellian distribution with a full loss cone, integrated over the same angular interval.

Figure 4. a) Number flux across energies as observed at the footprint of field line $L = 4.71$ along which the chorus element propagates. b) Integrated number flux from the first panel. Time $t = 0$ corresponds to the start of the chorus element.

tion for nonlinear chorus growth, the strong scattering can transport particles from a high-PSD, high-energy region to the loss cone where the bi-Maxwellian would have a lower PSD. It is evident, however, that it requires both very high amplitudes and high temperature anisotropies.

Resonant electrons which have fallen into the loss cone due to nonlinear scattering are expected to propagate down to atmospheric altitudes as prescribed by the adiabatic motion in the terrestrial magnetic field. Quasilinear diffusion from weaker waves is much slower than the nonlinear transport and does not have to be included, given the timescales considered in this paper. Following the PSD mapping method from Section 2, we plot the differential flux over energies and the total flux in Figure 4 (the dipole field model with a decreased value of surface strength, $B_{surf} = 2 \cdot 10^{-5}$ T, was retained for consistency with the scattering simulation). An intense burst of flux first appears near the energy level of 50 keV, corresponding to the resonance velocity of the first subpacket. The energy range then widens, reaching about 125 keV and extending down to 5 keV. The low-energy precipitating electrons have small parallel velocities and arrive up to about one second after the initiation of the chorus element. In Figure 4, the integrated number flux confirms the heavy precipitation related to the first subpacket, while the rest of the element's fine modulations does not translate to any clear structure in the pre-

cipitating flux. This loss of clear correlations is likely due to the varying time of flight of the resonant electrons and the phase space mixing of PSD perturbations at lower energies. Therefore, we expect that only the most prominent subpackets can result in micropulsation in diffuse auroras.

4 Conclusion

Simulation of perturbations of a hot electron distribution interacting with a parallel-propagating chorus element has shown that the nonlinear cyclotron resonance can break the strong diffusion limit and overfill the loss cone. However, very intense whistler waves with magnetic field amplitudes around 1% of the background field are necessary to cause overfilling comparable with flux measurement of (Zhang et al., 2022), which were identified as a consequence of Landau resonance with oblique whistler waves. Identification of these newly discovered effects of strong chorus wave packets in LEO spacecraft data is left for future studies.

The loss cone content precipitates into the atmosphere, showing a prominent flux peak associated with the strongest chorus subpacket. We expect this burst of electron flux to appear as a micropulse in measurements of auroral intensity. On the other hand, the rest of the subpacket structure with moderate wave amplitudes does not result in any clear flux pattern. This conclusion may explain the significant but low correlation between subpackets and auroral intensity peaks presented by Ozaki et al. (2018), suggesting that strong correlations should be expected only when very prominent, high-amplitude packets are present.

Despite the possibilities of current models that were demonstrated here, further research into the subpacket structure of chorus is necessary to develop more accurate wave-field models for prediction of microbursts and auroral intensities. This can be achieved in the future by studying the evolution of subpackets through multipoint, close separation spacecraft measurements (Santolík et al., 2004) and devising two-dimensional and three-dimensional semi-empirical chorus models that can capture the full complexity of amplitude modulations inside these emissions.

5 Open Research

The Van Allen Probe data are publicly available from the NASA's Space Physics Data Facility, repository https://spdf.gsfc.nasa.gov/pub/data/rbsp/. The test-particle code, along with the chorus wavefield model, can be accessed from `https://figshare.com/s/bee9aa0e13bdf7bb884e`, and the produced datasets are available from `https://figshare.com/s/98c0a959f6b0c11e3256`.

References

Albert, J. M., Artemyev, A. V., Li, W., Gan, L., & Ma, Q. (2021, June). Models of Resonant Wave-Particle Interactions. *J. Geophys. Res. Space Physics*, *126*(6), e29216. doi: 10.1029/2021JA029216

Allanson, O., Watt, C. E. J., Ratcliffe, H., Allison, H. J., Meredith, N. P., Bentley, S. N., ... Glauert, S. A. (2020, July). Particle-in-Cell Experiments Examine Electron Diffusion by Whistler-Mode Waves: 2. Quasi-Linear and Nonlinear Dynamics. *J. Geophys. Res. Space Physics*, *125*(7), e27949. doi: 10.1029/2020JA027949

Angelopoulos, V., Tsai, E., Bingley, L., Shaffer, C., Turner, D. L., Runov, A., ... Zhang, G. Y. (2020, July). The ELFIN Mission. *Space Sci. Rev.*, *216*(5), 103. doi: 10.1007/s11214-020-00721-7

Baker, D. N. (2021, December). Wave-particle interaction effects in the Van Allen belts. *Earth Planets Space*, *73*(1), 189. doi: 10.1186/s40623-021-01508-y

Breneman, A. W., Crew, A., Sample, J., Klumpar, D., Johnson, A., Agapitov, O., ... Kletzing, C. A. (2017, November). Observations Directly Linking Relativistic Electron Microbursts to Whistler Mode Chorus: Van Allen Probes and FIREBIRD II. *Geophys. Res. Lett.*, *44*, 11,265-11,272. doi: 10.1002/2017GL075001

Crabtree, C., Tejero, E., Ganguli, G., Hospodarsky, G. B., & Kletzing, C. A. (2017). Bayesian spectral analysis of chorus subelements from the van allen probes. *J. Geophys. Res. Space Physics*, *122*(6), 6088-6106. doi: 10.1002/2016JA023547

da Silva, C. L., Denton, R. E., Hudson, M. K., Millan, R. M., Liu, K., & Bortnik, J. (2018, June). Test-Particle Simulations of Linear and Nonlinear Interactions Between a 2-D Whistler-Mode Wave Packet and Radiation Belt Electrons. *Geophys. Res. Lett.*, *45*(11), 5234-5245. doi: 10.1029/2018GL077877

Foster, J. C., Erickson, P. J., Omura, Y., Baker, D. N., Kletzing, C. A., & Claudepierre, S. G. (2017, January). Van Allen Probes observations of prompt MeV radiation belt electron acceleration in nonlinear interactions with VLF chorus. *J. Geophys. Res. Space Physics*, *122*(1), 324-339. doi: 10.1002/2016JA023429

Hanzelka, M., Santolík, O., Omura, Y., & Kolmašová, I. (2021, September). Measurability of the Nonlinear Response of Electron Distribution Function to Chorus Emissions in the Earth's Radiation Belt. *J. Geophys. Res. Space Physics*, *126*(9), e29624. doi: 10.1029/2021JA029624

Hanzelka, M., Santolík, O., Omura, Y., Kolmašová, I., & Kletzing, C. A. (2020, August). A Model of the Subpacket Structure of Rising Tone Chorus Emissions. *J. Geophys. Res. Space Physics*, *125*(8), e28094. doi: 10.1029/2020JA028094

Higuera, A. V., & Cary, J. R. (2017, May). Structure-preserving second-order integration of relativistic charged particle trajectories in electromagnetic fields. *Phys. Plasmas*, *24*(5), 052104. doi: 10.1063/1.4979989

Hikishima, M., Omura, Y., & Summers, D. (2010, April). Microburst precipitation of energetic electrons associated with chorus wave generation. *Geophys. Res. Lett.*, *37*(7), L07103. doi: 10.1029/2010GL042678

Hiraga, R., & Omura, Y. (2020, February). Acceleration mechanism of radiation belt electrons through interaction with multi-subpacket chorus waves. *Earth Planets Space*, *72*(1), 21. doi: 10.1186/s40623-020-1134-3

Hsieh, Y.-K., Omura, Y., & Kubota, Y. (2022, January). Energetic Electron Precipitation Induced by Oblique Whistler Mode Chorus Emissions. *J. Geophys. Res. Space Physics*, *127*(1), e29583. doi: 10.1029/2021JA029583

Kawamura, M., Sakanoi, T., Fukizawa, M., Miyoshi, Y., Hosokawa, K., Tsuchiya, F., ... Brändström, U. (2021, September). Simultaneous Pulsating Aurora and Microburst Observations With Ground-Based Fast Auroral Imagers and CubeSat FIREBIRD-II. *Geophys. Res. Lett.*, *48*(18), e94494. doi: 10.1029/2021GL094494

Kennel, C. F., & Petschek, H. E. (1966, January). Limit on Stably Trapped Particle

Fluxes. *J. Geophys. Res.*, *71*, 1-28.

Kubota, Y., & Omura, Y. (2018, June). Nonlinear Dynamics of Radiation Belt Electrons Interacting With Chorus Emissions Localized in Longitude. *J. Geophys. Res. Space Physics*, *123*(6), 4835-4857. doi: 10.1029/2017JA025050

Li, W., Thorne, R. M., Bortnik, J., Shprits, Y. Y., Nishimura, Y., Angelopoulos, V., . . . Bonnell, J. W. (2011, July). Typical properties of rising and falling tone chorus waves. *Geophys. Res. Lett.*, *38*(14), L14103. doi: 10.1029/2011GL047925

Lorentzen, K. R., Blake, J. B., Inan, U. S., & Bortnik, J. (2001, April). Observations of relativistic electron microbursts in association with VLF chorus. *J. Geophys. Res.*, *106*(A4), 6017-6028. doi: 10.1029/2000JA003018

Miyoshi, Y., Saito, S., Kurita, S., Asamura, K., Hosokawa, K., Sakanoi, T., . . . Blake, J. B. (2020, November). Relativistic Electron Microbursts as High-Energy Tail of Pulsating Aurora Electrons. *Geophys. Res. Lett.*, *47*(21), e90360. doi: 10.1029/2020GL090360

Nunn, D., & Omura, Y. (2015, April). A computational and theoretical investigation of nonlinear wave-particle interactions in oblique whistlers. *J. Geophys. Res. Space Physics*, *120*(4), 2890-2911. doi: 10.1002/2014JA020898

Omura, Y. (2021, April). Nonlinear wave growth theory of whistler-mode chorus and hiss emissions in the magnetosphere. *Earth Planets Space*, *73*(1), 95. doi: 10.1186/s40623-021-01380-w

Ozaki, M., Shiokawa, K., Miyoshi, Y., Hosokawa, K., Oyama, S., Yagitani, S., . . . Shinohara, I. (2018, November). Microscopic Observations of Pulsating Aurora Associated With Chorus Element Structures: Coordinated Arase Satellite-PWING Observations. *Geophys. Res. Lett.*, *45*(22), 12,125-12,134. doi: 10.1029/2018GL079812

Santolík, O. (2008, July). New results of investigations of whistler-mode chorus emissions. *Nonlin. Processes Geophys.*, *15*(4), 621-630. doi: 10.5194/npg-15-621-2008

Santolík, O., Gurnett, D., & Pickett, J. (2004, July). Multipoint investigation of the source region of storm-time chorus. *Ann. Geophys.*, *22*, 2555-2563. doi: 10.5194/angeo-22-2555-2004

Santolík, O., Gurnett, D. A., Pickett, J. S., Parrot, M., & Cornilleau-Wehrlin, N.

(2003, July). Spatio-temporal structure of storm-time chorus. *J. Geophys. Res. Space Physics*, *108*, 1278. doi: 10.1029/2002JA009791

Santolík, O., Kletzing, C. A., Kurth, W. S., Hospodarsky, G. B., & Bounds, S. R. (2014, January). Fine structure of large-amplitude chorus wave packets. *Geophys. Res. Lett.*, *41*, 293-299. doi: 10.1002/2013GL058889

Santolík, O., Parrot, M., & Lefeuvre, F. (2003, February). Singular value decomposition methods for wave propagation analysis. *Radio Sci.*, *38*, 10-1. doi: 10.1029/2000RS002523

Sauvaud, J. A., Moreau, T., Maggiolo, R., Treilhou, J. P., Jacquey, C., Cros, A., ... Gangloff, M. (2006, April). High-energy electron detection onboard DEMETER: The IDP spectrometer, description and first results on the inner belt. *Planet. Space Sci.*, *54*(5), 502-511. doi: 10.1016/j.pss.2005.10.019

Summers, D., Ni, B., & Meredith, N. P. (2007, April). Timescales for radiation belt electron acceleration and loss due to resonant wave-particle interactions: 2. Evaluation for VLF chorus, ELF hiss, and electromagnetic ion cyclotron waves. *J. Geophys. Res. Space Physics*, *112*(A4), A04207. doi: 10.1029/2006JA011993

Summers, D., Thorne, R. M., & Xiao, F. (1998, September). Relativistic theory of wave-particle resonant diffusion with application to electron acceleration in the magnetosphere. *J. Geophys. Res.*, *103*(A9), 20487-20500. doi: 10.1029/98JA01740

Taubenschuss, U., Santolík, O., Graham, D. B., Fu, H., Khotyaintsev, Y. V., & Le Contel, O. (2015, October). Different types of whistler mode chorus in the equatorial source region. *Geophys. Res. Lett.*, *42*(20), 8271-8279. doi: 10.1002/2015GL066004

Teng, S., Tao, X., & Li, W. (2019, April). Typical Characteristics of Whistler Mode Waves Categorized by Their Spectral Properties Using Van Allen Probes Observations. *Geophys. Res. Lett.*, *46*(7), 3607-3614. doi: 10.1029/2019GL082161

Tsurutani, B. T., Lakhina, G. S., & Verkhoglyadova, O. P. (2013, May). Energetic electron (>10 keV) microburst precipitation, ∼5-15 s X-ray pulsations, chorus, and wave-particle interactions: A review. *Journal of Geophysical Research (Space Physics)*, *118*(5), 2296-2312. doi: 10.1002/jgra.50264

Zenitani, S., & Umeda, T.   (2018, November).   On the Boris solver in particle-in-cell simulation. *Phys. Plasmas*, *25*(11), 112110. doi: 10.1063/1.5051077

Zhang, X. J., Agapitov, O., Artemyev, A. V., Mourenas, D., Angelopoulos, V., Kurth, W. S., . . . Hospodarsky, G. B.   (2020, October).   Phase Decoherence Within Intense Chorus Wave Packets Constrains the Efficiency of Nonlinear Resonant Electron Acceleration.   *Geophys. Res. Lett.*, *47*(20), e89807.   doi: 10.1029/2020GL089807

Zhang, X. J., Artemyev, A., Angelopoulos, V., Tsai, E., Wilkins, C., Kasahara, S., . . . Matsuoka, A.   (2022, March).   Superfast precipitation of energetic electrons in the radiation belts of the Earth.   *Nat. Commun.*, *13*.   doi: 10.1038/s41467-022-29291-8